# Amazonian Biomass Burning Drives Regional Air Pollution and Premature Mortality in South America

Alejandro Casallas[1,2], Tatiana Medina[3], Brendan Steffens[2], Camila Jimenez-Saenz[4], Franz Antezana-Lopez[5,6], Ellie Anne Lopez-Barrera[7], Carlos Plata[8], Ricardo Arenas[9], Léo Dürst[10], Stijn Hantson[11], Luis Carlos Belalcazar[3], and Andrea Pozzer[2,12]

[1]Institute of Science and Technology Austria, Klosterneuburg, Austria, 3400
[2]Atmospheric Chemistry Department, Max-Planck Institute for Chemistry, Mainz, Germany, 55128
[3]Universidad Nacional de Colombia, Bogotá, Colombia, 111321
[4]Facultad de Estudios Ambientales y Rurales, Pontificia Universidad Javeriana, Bogotá, Colombia. 111711
[5]School of Instrumentation Science and Optoelectronic Engineering, Beihang University, Beijing, China, 100191
[6]Hangzhou International Innovation Institute, Beihang University, Hangzhou, China, 100191
[7]Instituto de Estudios y Servicios Ambientales, Universidad Sergio Arboleda, Bogotá, Colombia, 111711
[8]EM Normandie Business School, Metis Lab, Le Havre, France, 76600
[9]Research Center in Philosophy and Law, Universidad Externado de Colombia, Bogotá, Colombia, 111711
[10]Institute for Atmospheric and Climate Science, ETH Zürich, Zürich, Switzerland, 8092
[11]School of Sciences and Engineering, Universidad del Rosario, Bogotá, Colombia
[12]Climate and Atmosphere Research Center, The Cyprus Institute, Nicosia, Cyprus, 2021

October 15, 2026

## Contents of this file

1. Introduction
2. Tables
3. Figures

# 1 Introduction

This Supplementary Information provides additional analyses, model evaluation results, and supporting figures and tables that complement the findings presented in the main manuscript. The material expands upon the characterization of Amazonian fire activity, the associated atmospheric pollution patterns across South America, and the performance of the modeling framework used to quantify air-quality and health impacts. Figures in this file are ordered to match the sequence in which they are first cited in the main text.

Table S1 summarizes the air-quality monitoring stations used throughout the study. The table provides the geographic location of each urban site, including latitude and longitude coordinates. These stations form the basis for the city-scale analyses of plume transport, air-quality variability, and model performance presented in both the main manuscript and the supplementary figures.

Figure S1 depicts the study and simulation domain and geographic context of the analysis over South America, including its elevation, which includes the Andes mountain range along the western margin and the low-lying Amazon Basin in the interior. Figure S2 shows the four alternative baseline estimates ($M = 1$–$4$) computed for each city and year in the baseline method, illustrating how little the baseline depends on the choice of $M$. Figure S3 shows the spatial distribution of annual VIIRS fire hotspot detections across South America from 2013 to 2023, illustrating the interannual variability of fire activity referenced in the Data and Methods section.

Figures S4-S11 summarize model and dataset performance against ground-based observations using a range of statistical metrics, including mean bias (MB), normalized mean bias (NMB), root mean square error (RMSE), correlation coefficients, FAC2, index of agreement (IOA), hit rates, false alarm ratios, and probability of detection. These figures provide the evidence underlying the evaluation of the CAMS reanalysis, the ACAG dataset, and the WRF-Chem simulation presented as the first Results subsection of the manuscript.

Figures S12 and S13 present the multi-year average seasonal evolution of the pollution plumes for $PM_{10}$ and total column carbon monoxide (TCCO). Figures S14-S16 provide an overview of the spatial and temporal evolution of fire activity and particulate matter concentrations (from the pollution plumes) across South America during the 2013–2023 period, including annual $PM_{2.5}$, $PM_{10}$, and TCCO fields. Figure S17 presents a multi-year composite comparison of Amazon-origin plume-derived $PM_{2.5}$ and $PM_{10}$ against VIIRS fire hotspot distributions, both within the Amazon Basin and across South America, providing an independent consistency check on the attribution of the identified plumes to biomass burning. Figures S18 and S19 present the seasonal and monthly variability of $PM_{2.5}$ concentrations observed at the urban locations analyzed in this study.

Figures S20 and S21 examine the relationships between fire occurrence and atmospheric composition indicators, including $PM_{10}$ and TCCO, while Figures S22 and S23 represent the correlation of $PM_{2.5}$ and TCCO, and $PM_{10}$, respectively. This allows an assessment of the seasonal coupling between biomass burning and regional air pollution. Figure S24 provides the distance frequency from the pollution plume onset and the cities studied. Figures S25 and S26 are monthly sensitivity simulations used to isolate the contribution of Amazonian fires relative to all South American fire emissions. Figure S27 presents $PM_{2.5}$-attributable mortality per capita by country for the baseline scenario, highlighting health burdens that are disproportionate to population size. Figure S28 compares annual hotspot densities within protected areas and non-protected areas across Amazonian countries between 2013 and 2023, providing additional context for the role of land-use governance and conservation strategies in modulating fire occurrence across the basin.

## 2 Tables

This section includes all supplementary tables referenced in the main text.

Table S1: Location of the air-quality monitoring stations used in this study.

| Country | City | Latitude | Longitude |
|---|---|---|---|
| Bolivia | Cochabamba | -17.39 | -66.16 |
| Brazil | São Paulo | -23.62 | -46.45 |
| Brazil | Vitória | -20.32 | -40.34 |
| Chile | Santiago | -33.46 | -70.66 |
| Colombia | Bogotá | 4.71 | -73.82 |
| Ecuador | Quito | -0.19 | -78.54 |
| French Guiana | Cayenne | 4.94 | -52.33 |
| Peru | Lima | -12.05 | -77.05 |
| Uruguay | Montevideo | -34.66 | -55.60 |

# 3 Figures

This section includes all supplementary figures referenced in the main text, ordered to match their first citation in the Data and Methods and Results sections.

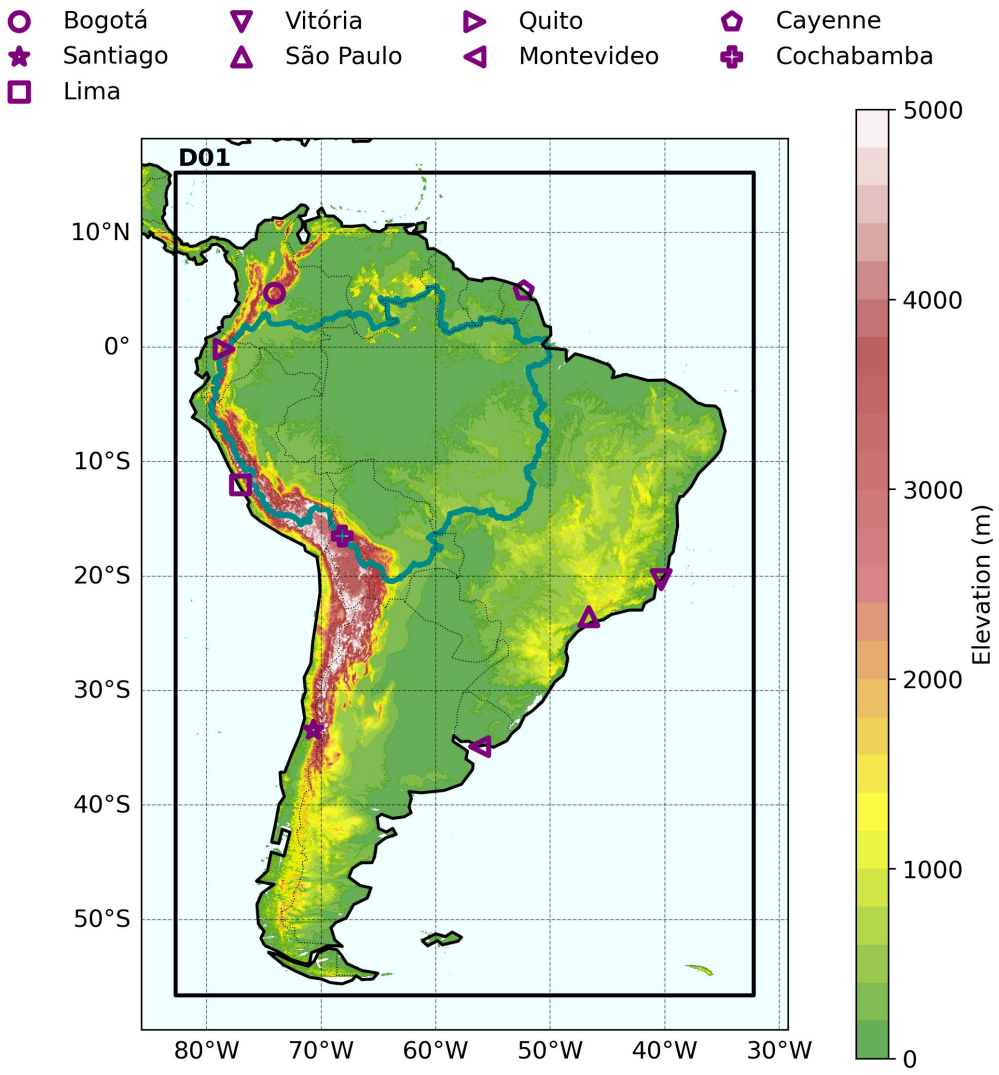



Figure S1: Study domain (D01, black rectangle) and geographic context of the analysis over South America. Shading indicates surface elevation (m), highlighting the Andes mountain range along the western margin and the low-lying Amazon Basin in the interior. The green outline delineates the Amazon Basin. Purple markers indicate the locations of the selected cities used for air-quality and plume-transport analyses.

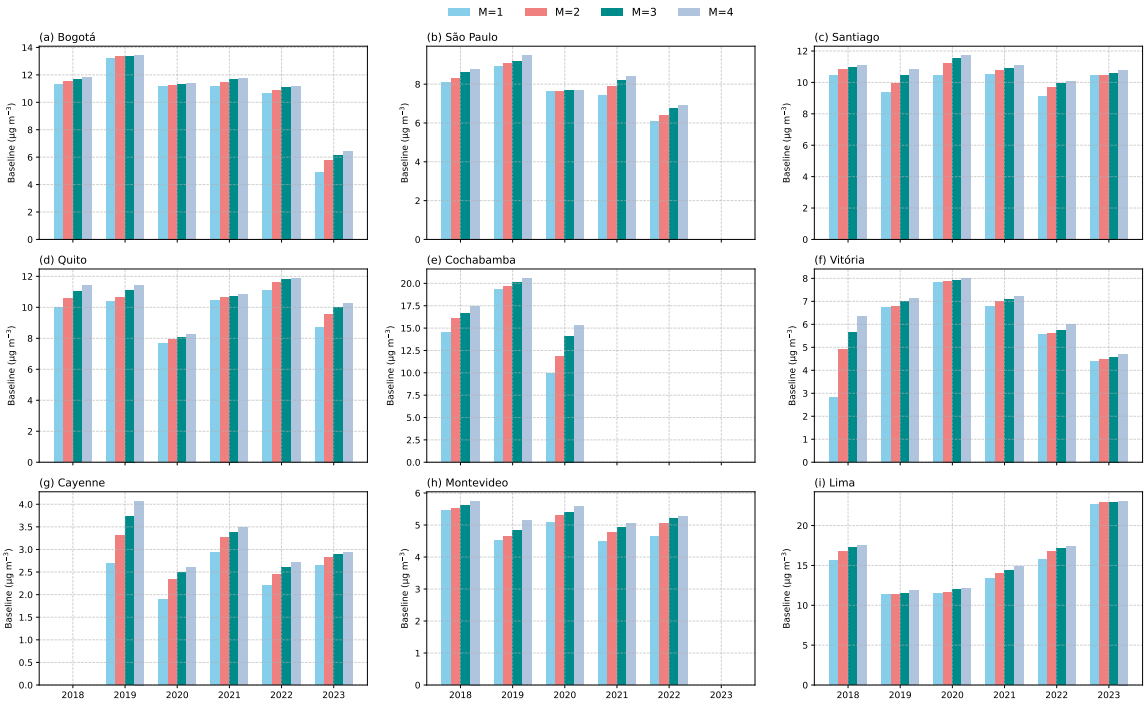



Figure S2: Annual baseline particulate matter concentrations ($\mu$g m$^{-3}$) computed from the surface station observations ($PM_{2.5}$; $PM_{10}$ for Cochabamba) for each study city with the four alternative baseline definitions used in the baseline method, in which the baseline is the mean of the $M$ lowest weekly concentrations of the year, with $M = 1$, 2, 3, and 4 (see legend; $M = 2$ is used in the main analysis). Each panel corresponds to one city: (a) Bogotá, (b) São Paulo, (c) Santiago, (d) Quito, (e) Cochabamba, (f) Vitória, (g) Cayenne, (h) Montevideo, and (i) Lima. Bars are shown for the years displayed (2018–2023); missing bars indicate years for which no baseline is available. Values are $PM_{2.5}$ except for Cochabamba, where $PM_{10}$ is used.

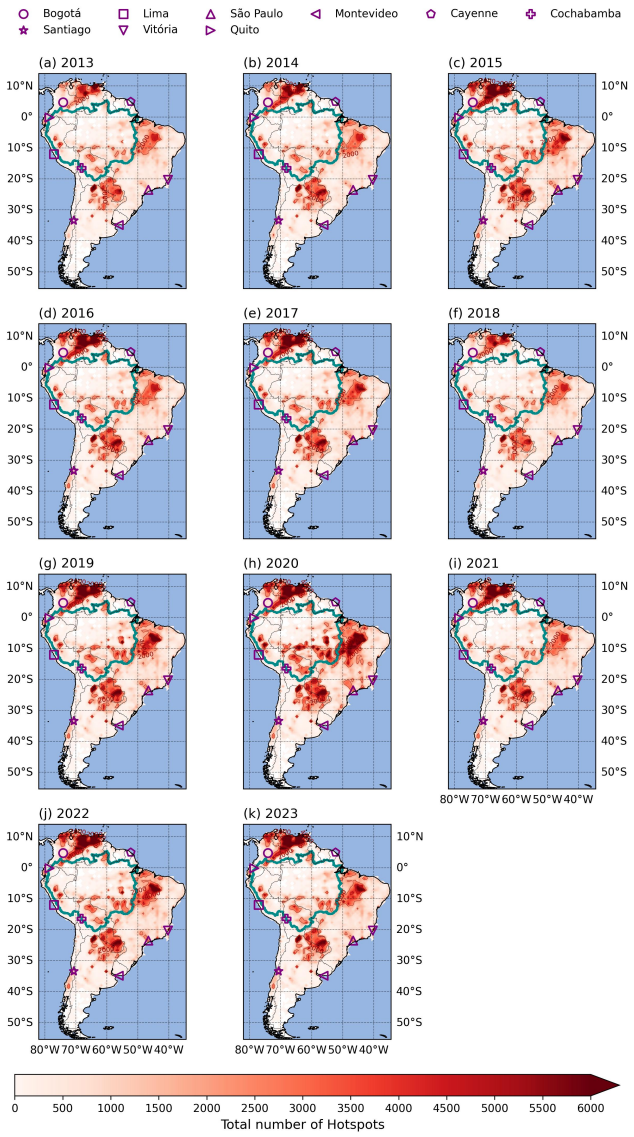



Figure S3: Spatial distribution of annual VIIRS fire hotspot detections across South America from 2013 to 2023. Panels (a)-(k) show the total number of hotspot detections recorded in each year, from 2013 (a) to 2023 (k). The green outline indicates the biogeographic Amazon Basin, while symbols denote the urban locations analyzed in this study.

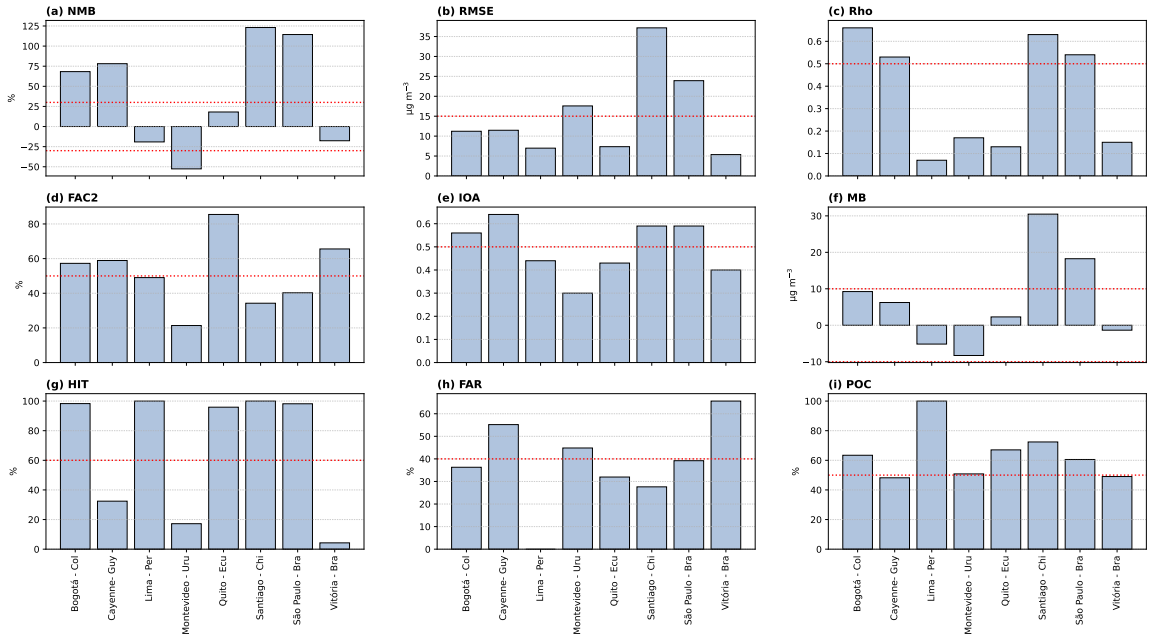



Figure S4: Statistical evaluation of CAMS $PM_{2.5}$ concentrations against surface observations at the daily scale for the eight cities with $PM_{2.5}$ observations (all study cities except Cochabamba, whose $PM_{10}$ evaluation is shown in Fig. S6). Performance metrics include normalized mean bias (NMB), root mean square error (RMSE), Spearman correlation coefficient ($\rho$), fraction within a factor of two (FAC2), index of agreement (IOA), mean bias (MB), hit rate (HIT), false alarm ratio (FAR), and probability of detection (POC). Each panel shows one metric, arranged in three rows of three: (a) NMB, (b) RMSE, (c) $\rho$, (d) FAC2, (e) IOA, (f) MB, (g) HIT, (h) FAR, and (i) POC, with one bar per city (city–country labels on the lower axes). Red dotted lines indicate commonly used benchmark values where applicable.

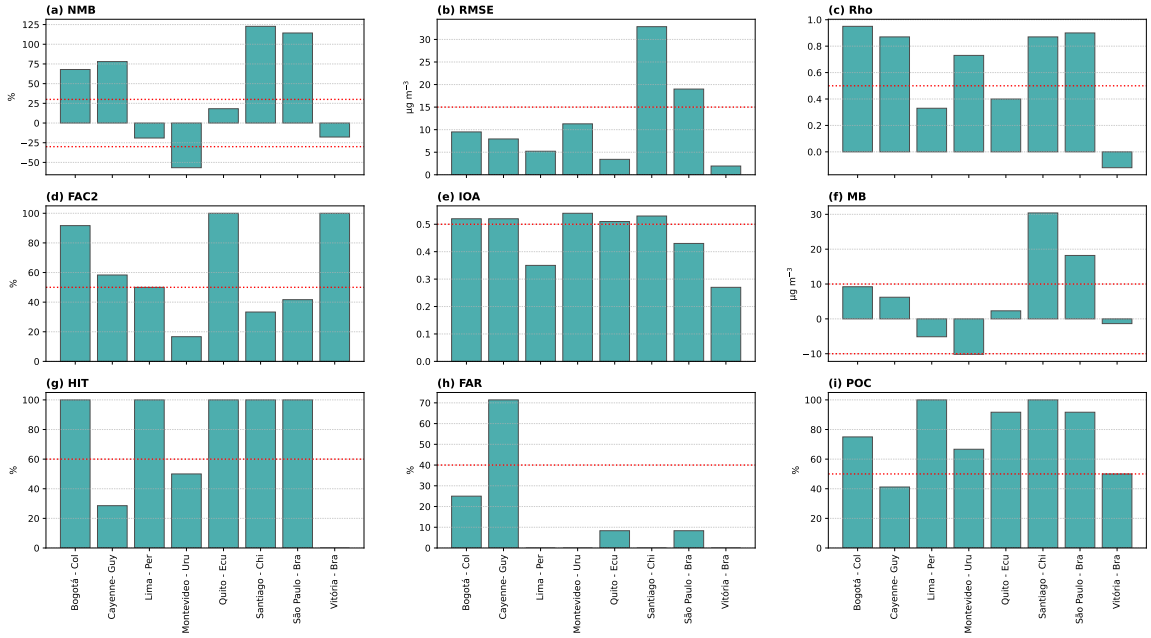



Figure S5: Statistical evaluation of CAMS $PM_{2.5}$ concentrations against surface observations at the monthly scale for the eight cities with $PM_{2.5}$ observations (all study cities except Cochabamba, whose $PM_{10}$ evaluation is shown in Fig. S6). Each panel shows one metric, arranged in three rows of three: (a) NMB, (b) RMSE, (c) $\rho$, (d) FAC2, (e) IOA, (f) MB, (g) HIT, (h) FAR, and (i) POC, with one bar per city. Metric abbreviations are defined in the caption of Fig. S4. Red dotted lines indicate commonly used benchmark values where applicable.

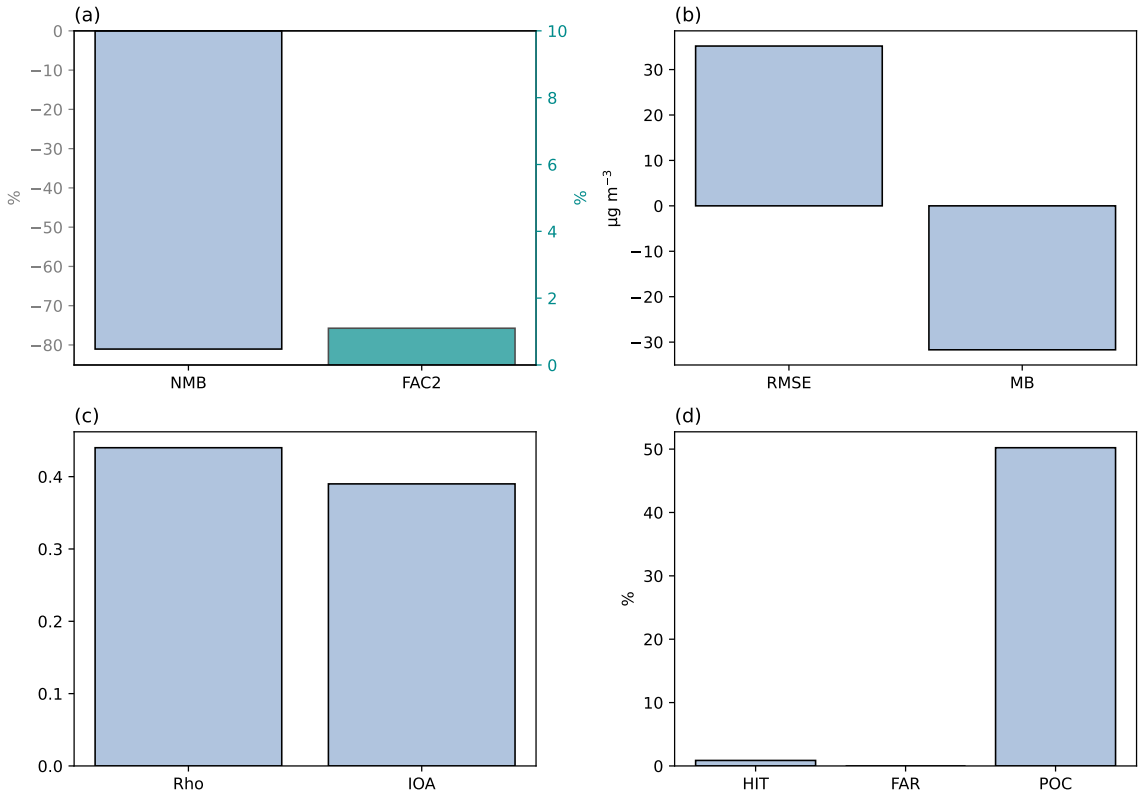



Figure S6: Statistical evaluation of CAMS $PM_{10}$ concentrations against surface observations in Cochabamba, Bolivia, at the daily time scale. Only one Bolivian location (Cochabamba; Table S1) is evaluated, so each bar represents one metric rather than one city. Panels show: (a) NMB (left axis) and FAC2 (right axis); (b) RMSE and MB; (c) $\rho$ and IOA; (d) HIT, FAR, and POC.

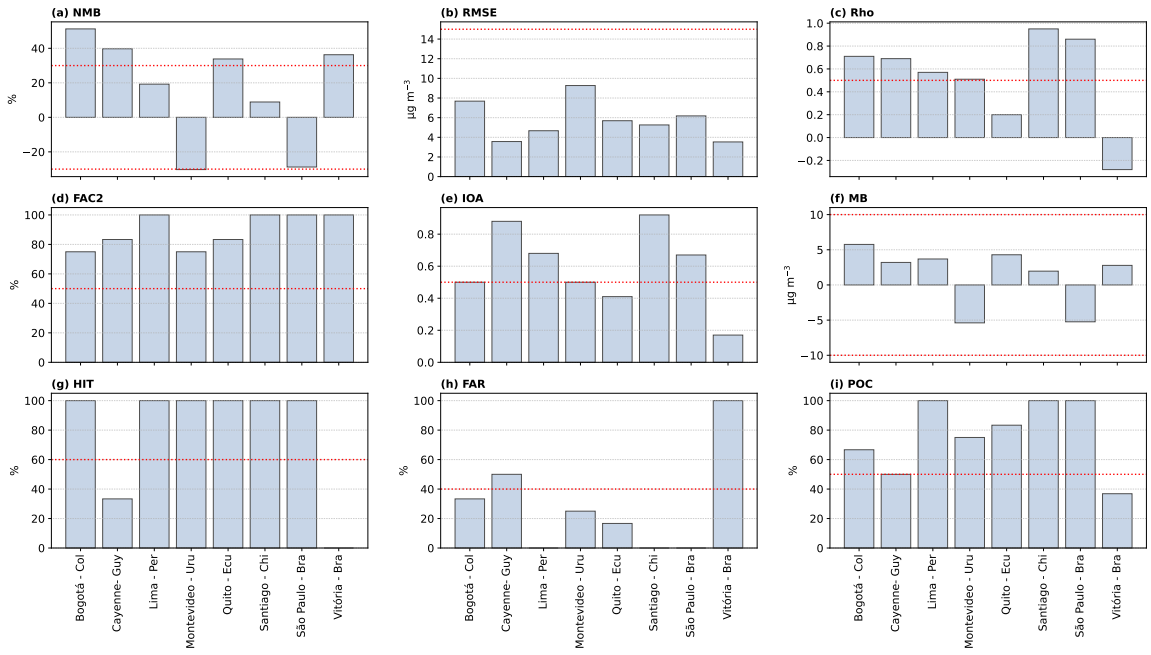



Figure S7: Statistical evaluation of monthly mean $PM_{2.5}$ concentrations from the ACAG dataset against surface monitoring stations for the eight cities with $PM_{2.5}$ observations (all study cities except Cochabamba, whose $PM_{10}$ evaluation is shown in Fig. S6). Each panel shows one metric, arranged in three rows of three: (a) NMB, (b) RMSE, (c) $\rho$, (d) FAC2, (e) IOA, (f) MB, (g) HIT, (h) FAR, and (i) POC, with one bar per city. Metric abbreviations are defined in the caption of Fig. S4. Red dotted lines indicate benchmark values used to assess model performance where applicable.

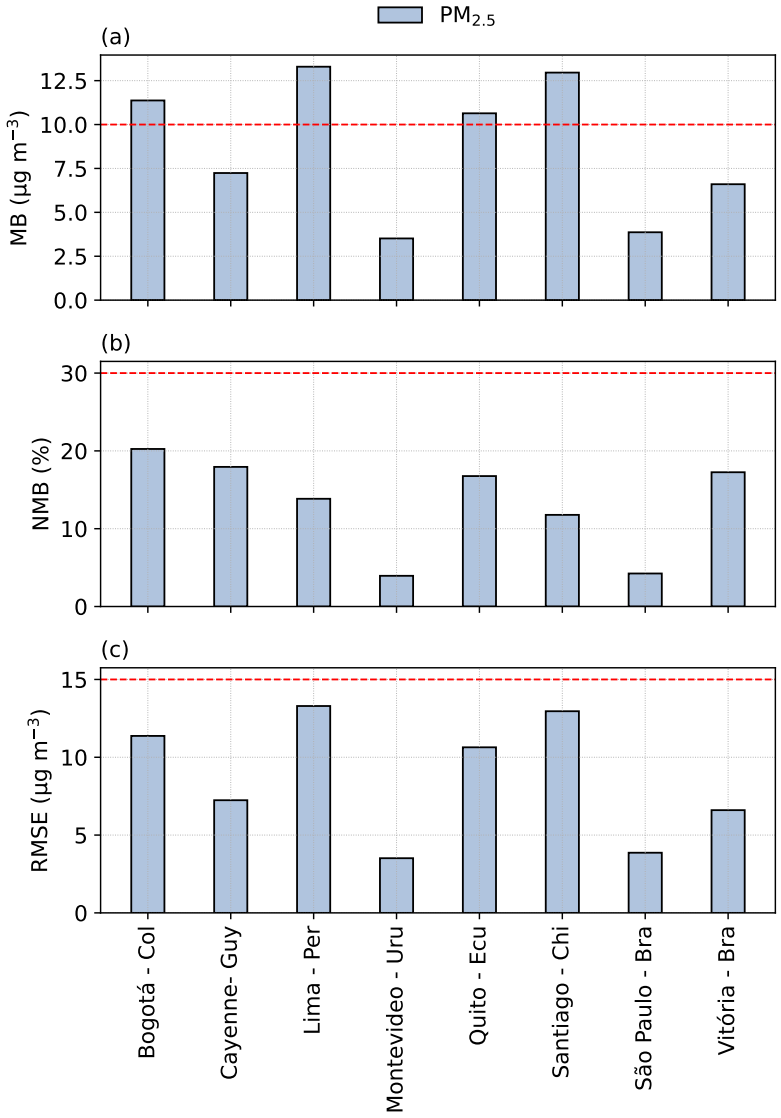



Figure S8: Statistical evaluation of annual mean $PM_{2.5}$ concentrations from the ACAG dataset against surface monitoring stations for the eight cities with $PM_{2.5}$ observations (all study cities except Cochabamba, whose $PM_{10}$ evaluation is shown in Fig. S6). Panels show (a) mean bias (MB), (b) normalized mean bias (NMB), and (c) root mean square error (RMSE), with one bar per city. Red dashed lines indicate benchmark values used to assess model performance.

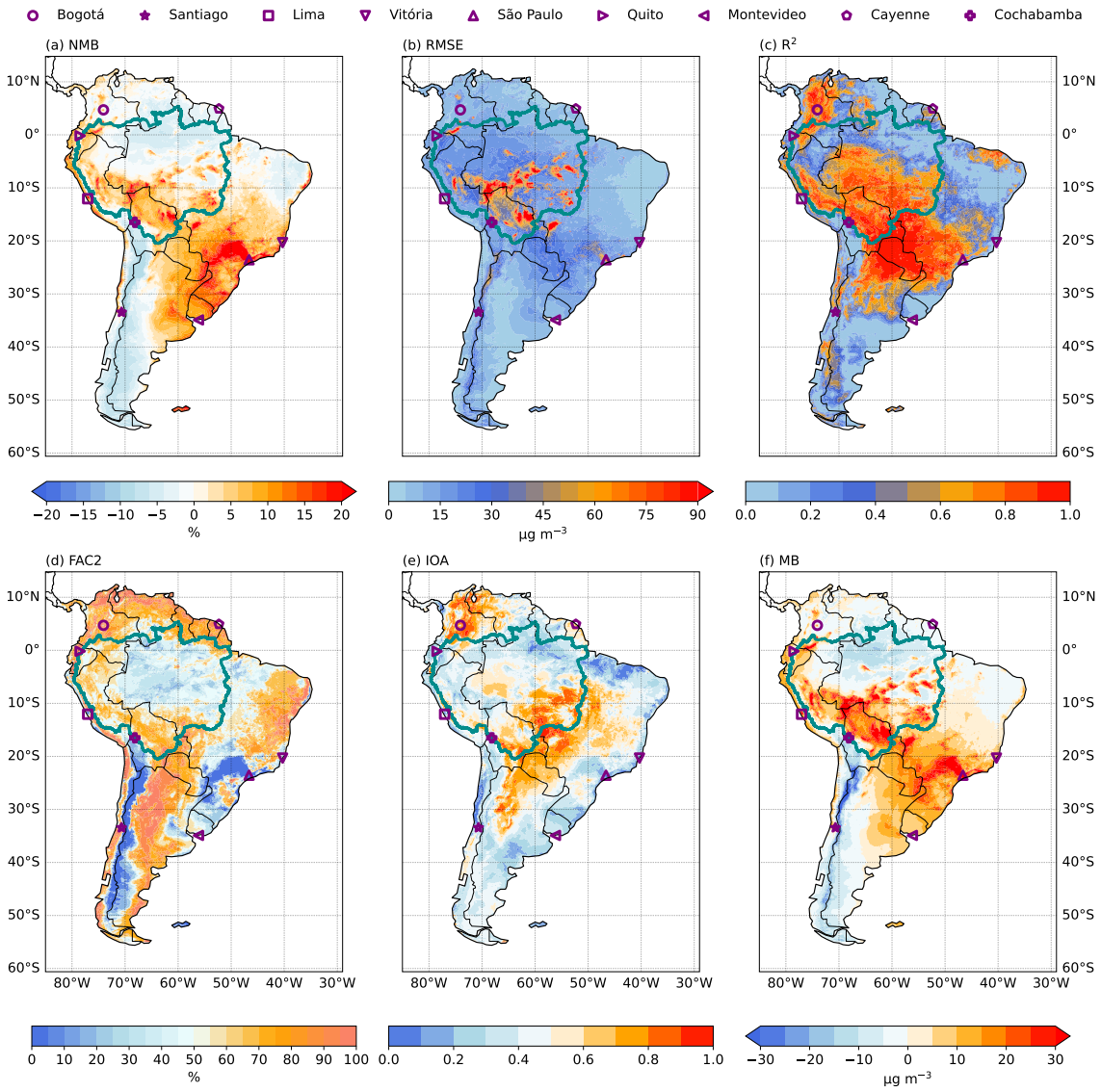



Figure S9: Spatial evaluation of monthly mean $PM_{2.5}$ concentrations simulated by WRF-Chem against the ACAG $PM_{2.5}$ dataset over South America. Performance metrics are (a) NMB, (b) RMSE, (c) $R^2$, (d) FAC2, (e) IOA, and (f) MB (abbreviations as in Fig. S4). Symbols indicate the urban locations analyzed in this study, while the green contour delineates the biogeographic Amazon Basin.

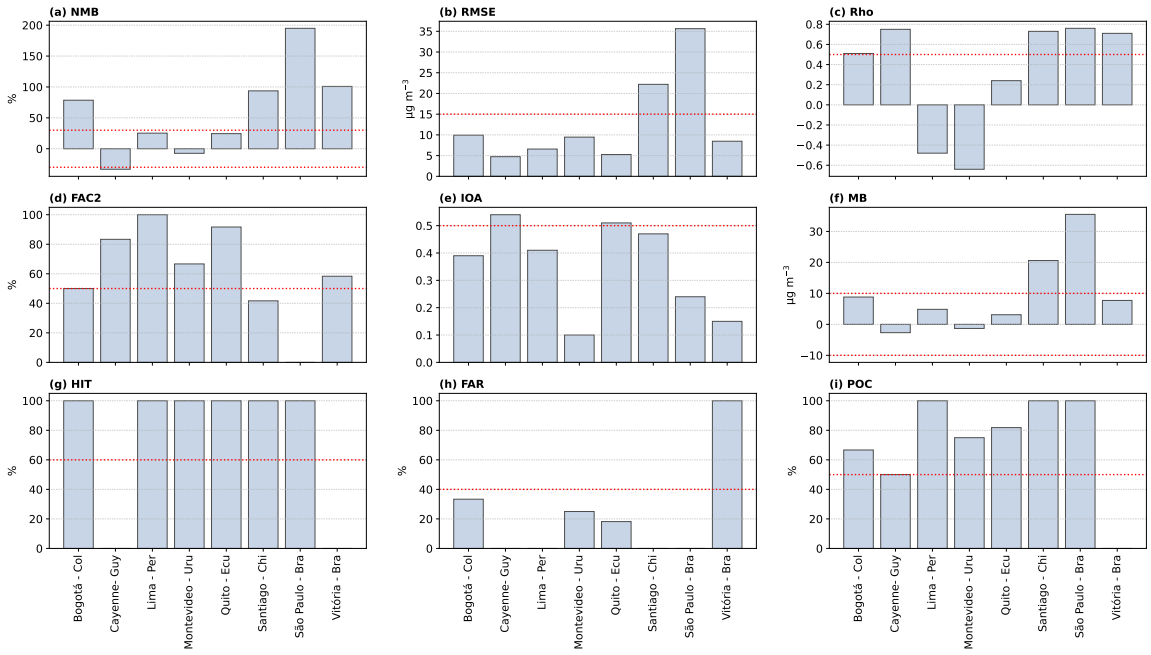



Figure S10: Statistical evaluation of monthly mean $PM_{2.5}$ concentrations simulated by WRF-Chem against surface monitoring observations for the eight cities with $PM_{2.5}$ observations (all study cities except Cochabamba, whose $PM_{10}$ evaluation is shown in Fig. S6). Each panel shows one metric, arranged in three rows of three: (a) NMB, (b) RMSE, (c) $\rho$, (d) FAC2, (e) IOA, (f) MB, (g) HIT, (h) FAR, and (i) POC, with one bar per city. Metric abbreviations are defined in the caption of Fig. S4. Red dotted lines indicate benchmark values commonly used to assess model performance.

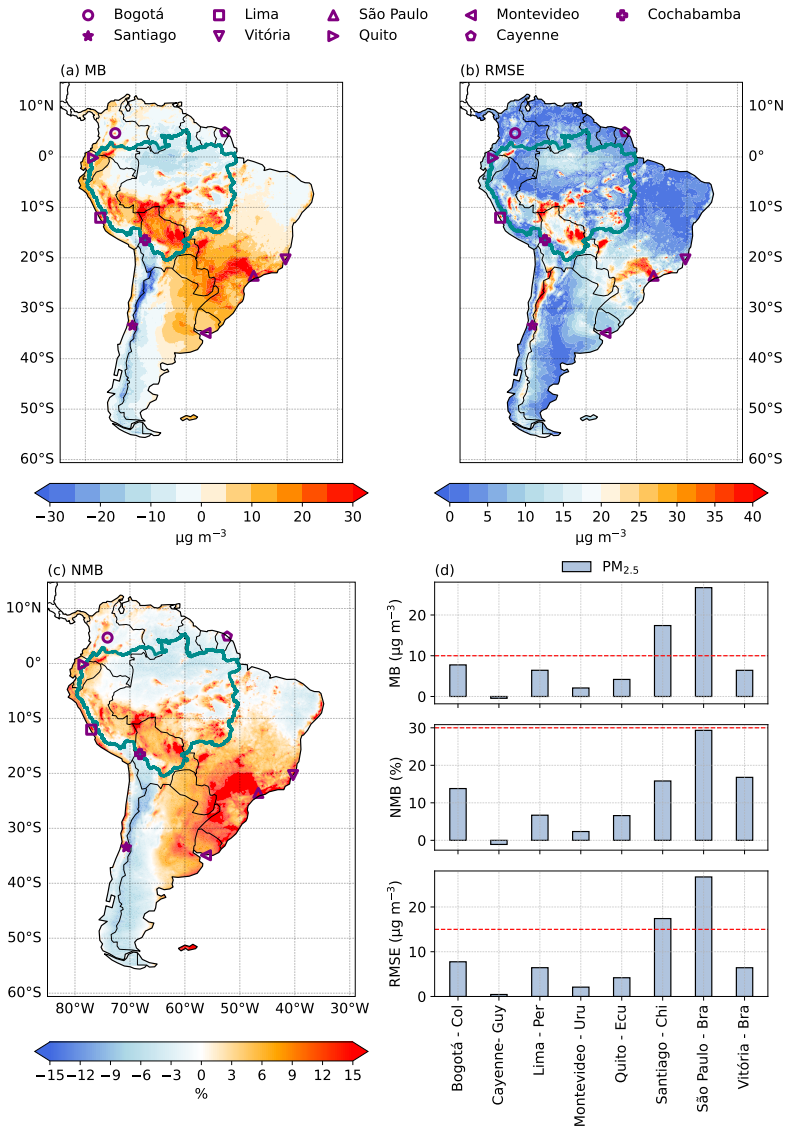



Figure S11: Evaluation of annual mean $PM_{2.5}$ concentrations simulated by WRF-Chem. Panels (a)-(c) show the spatial comparison between WRF-Chem and the ACAG $PM_{2.5}$ dataset across South America, including MB, RMSE, and NMB. The green contour delineates the biogeographic Amazon Basin, and symbols indicate the urban locations analyzed in this study. Panel (d) summarizes the comparison between annual mean WRF-Chem $PM_{2.5}$ concentrations and surface monitoring observations at the study cities, showing MB, NMB, and RMSE for the eight cities with $PM_{2.5}$ observations (one bar per city; abbreviations as in Fig. S4). Red dashed lines indicate benchmark values commonly used to assess model performance.

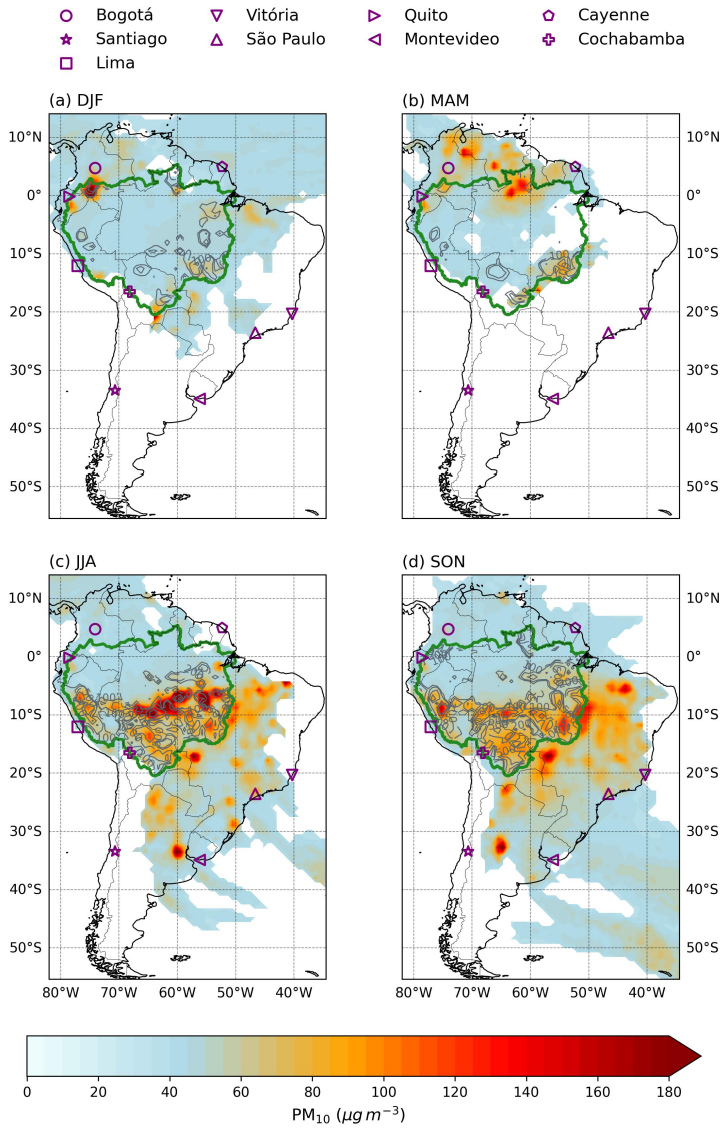



Figure S12: Seasonal multi-year mean (2013–2023) of $PM_{10}$ concentrations associated with Amazon-origin smoke plumes identified using the Lagrangian plume-tracking methodology. Shaded areas show the multi-year seasonal mean $PM_{10}$ concentrations linked to tracked plumes, while grey contours represent the seasonal mean fire hotspot distribution derived from VIIRS observations. Panels show (a) DJF, (b) MAM, (c) JJA, and (d) SON. The green outline denotes the biogeographic Amazon, and symbols mark the cities analyzed in this study.

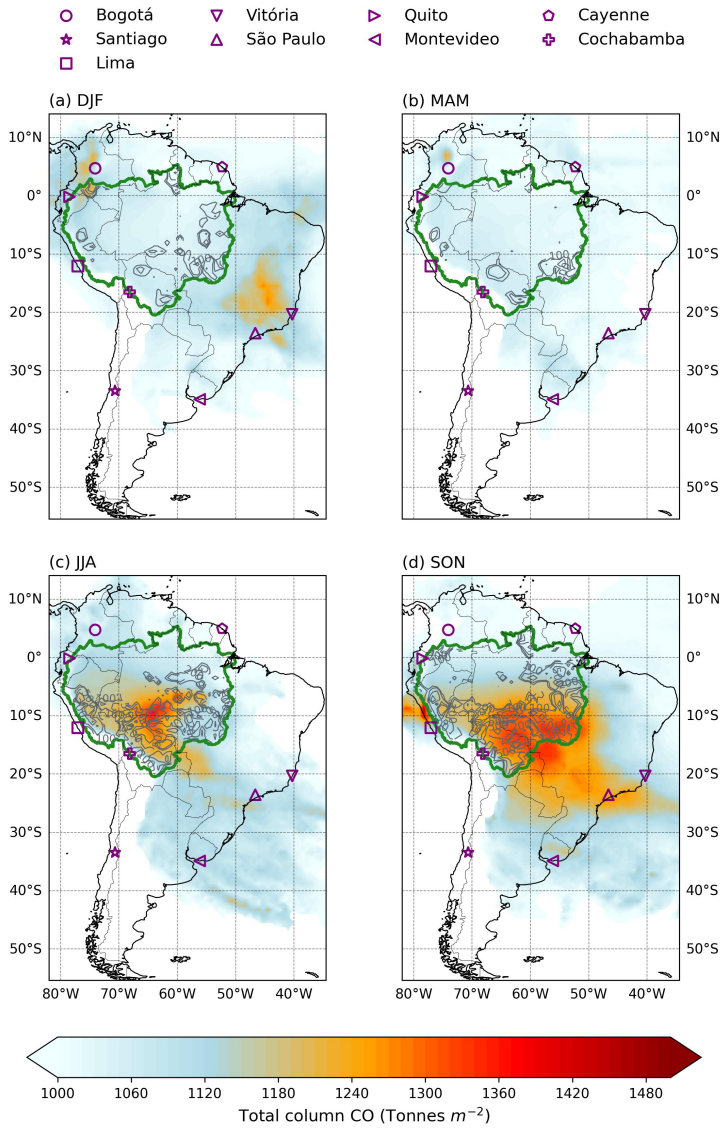



Figure S13: Seasonal multi-year mean (2013–2023) of TCCO concentrations associated with Amazon-origin smoke plumes identified using the Lagrangian plume-tracking methodology. Shaded areas show the multi-year seasonal mean TCCO concentrations linked to tracked plumes, while grey contours represent the seasonal mean fire hotspot distribution derived from VIIRS observations. Panels show (a) DJF, (b) MAM, (c) JJA, and (d) SON. The green outline denotes the biogeographic Amazon, and symbols mark the cities analyzed in this study.

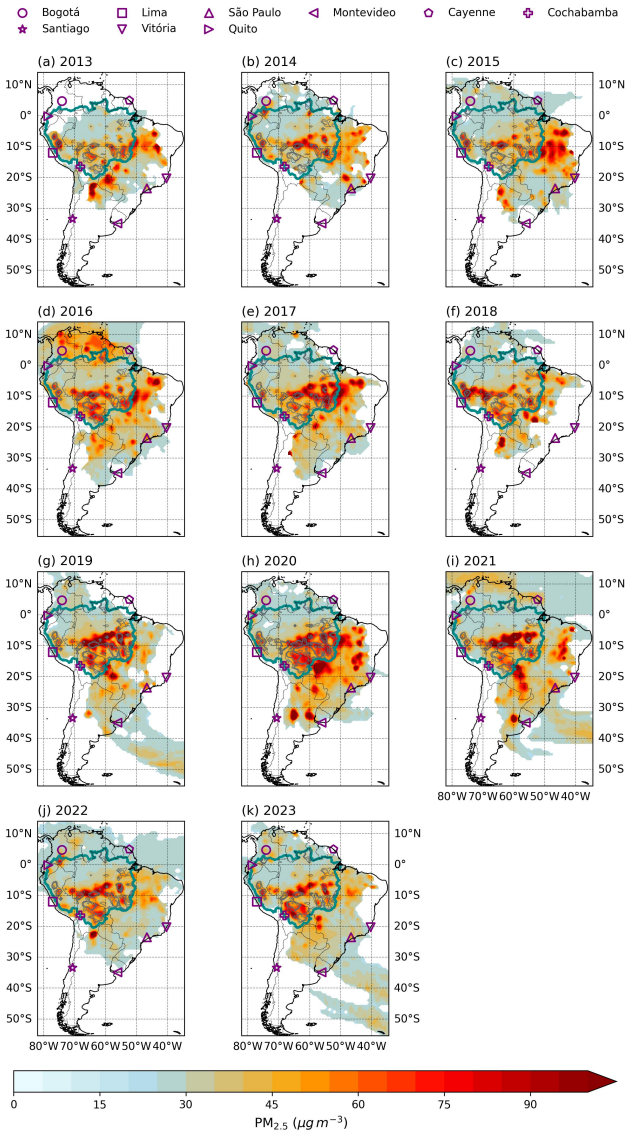



Figure S14: $PM_{2.5}$ annual mean occurrence of Amazonian smoke plumes identified using the Lagrangian plume-tracking methodology from 2013 to 2023. Panels (a)-(k) show individual years, from 2013 (a) to 2023 (k). Shaded areas represent the frequency of plume occurrence attributable to fires within the Amazon Basin, while grey contours indicate VIIRS fire hotspot detections. The green contour denotes the biogeographic Amazon, and symbols mark the cities included in the air-quality and health-impact analyses.

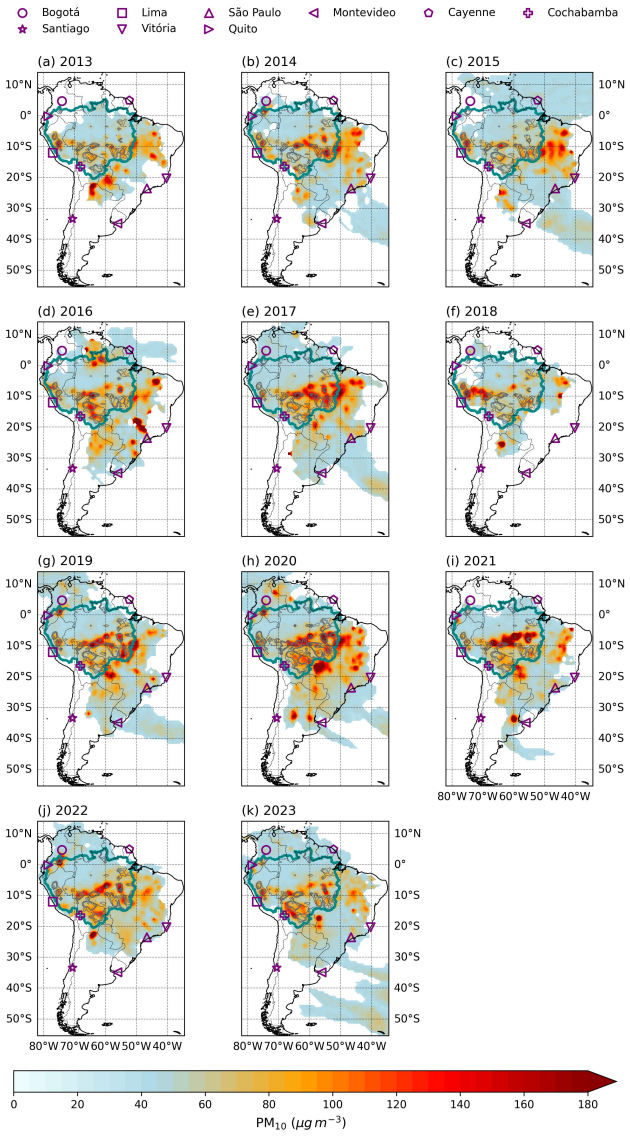



Figure S15: $PM_{10}$ annual mean occurrence of Amazonian smoke plumes identified using the Lagrangian plume-tracking methodology from 2013 to 2023. Panels (a)-(k) show individual years, from 2013 (a) to 2023 (k). Shaded areas represent the frequency of plume occurrence attributable to fires within the Amazon Basin, while grey contours indicate VIIRS fire hotspot detections. The green contour denotes the biogeographic Amazon, and symbols mark the cities included in the air-quality and health-impact analyses.

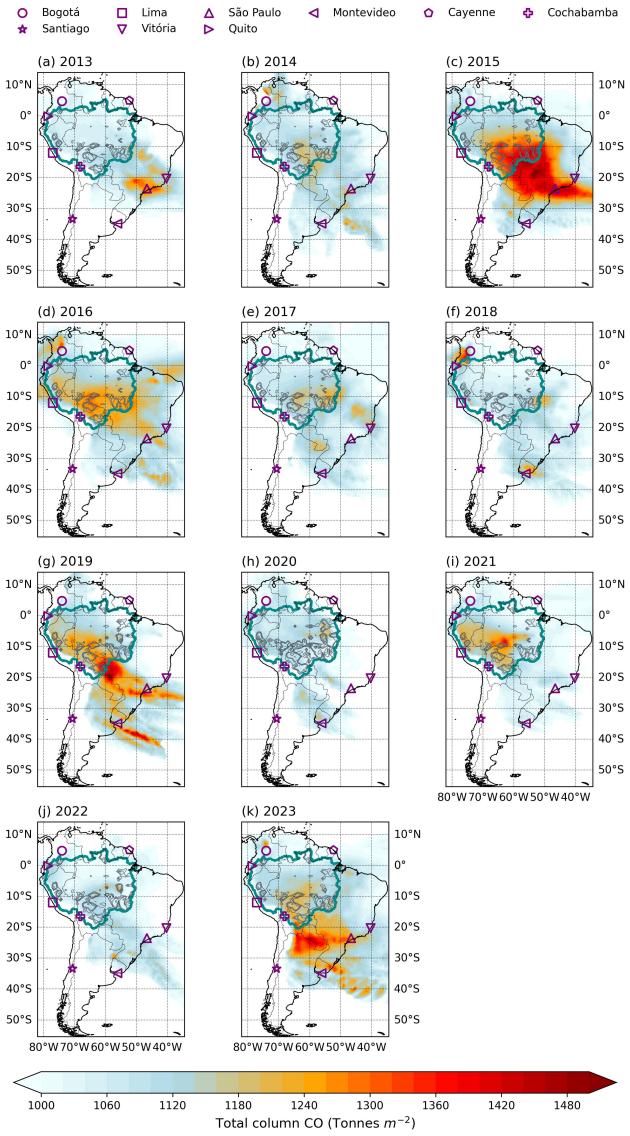



Figure S16: TCCO annual mean occurrence of Amazonian smoke plumes identified using the Lagrangian plume-tracking methodology from 2013 to 2023. Panels (a)-(k) show individual years, from 2013 (a) to 2023 (k). Shaded areas represent the frequency of plume occurrence attributable to fires within the Amazon Basin, while grey contours indicate VIIRS fire hotspot detections. The green contour denotes the biogeographic Amazon, and symbols mark the cities included in the air-quality and health-impact analyses.

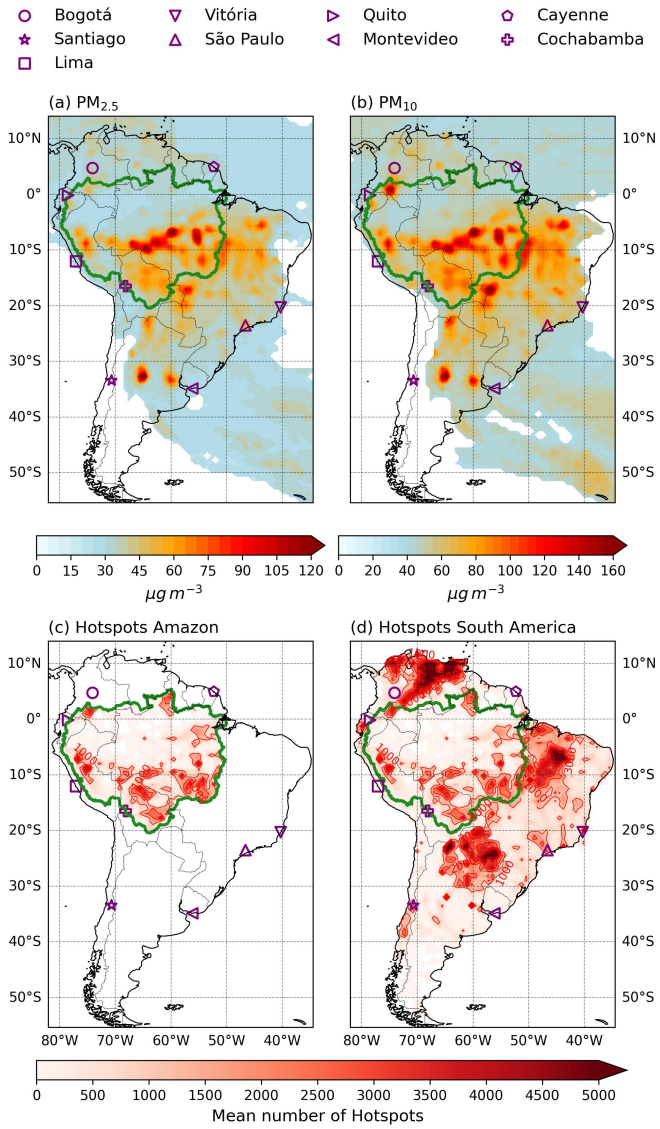



Figure S17: Multi-year composite of Amazonian smoke plumes and fire activity for the 2013-2023 period. Panels (a) and (b) show the average $PM_{2.5}$ and $PM_{10}$ concentrations associated with all plume events originating within the Amazon Basin and identified by the Lagrangian tracking methodology. Panels (c) and (d) show the mean spatial distribution of VIIRS fire hotspot detections within the Amazon Basin and across South America, respectively. The green outline represents the biogeographic Amazon Basin, while symbols denote the cities analyzed in this study.

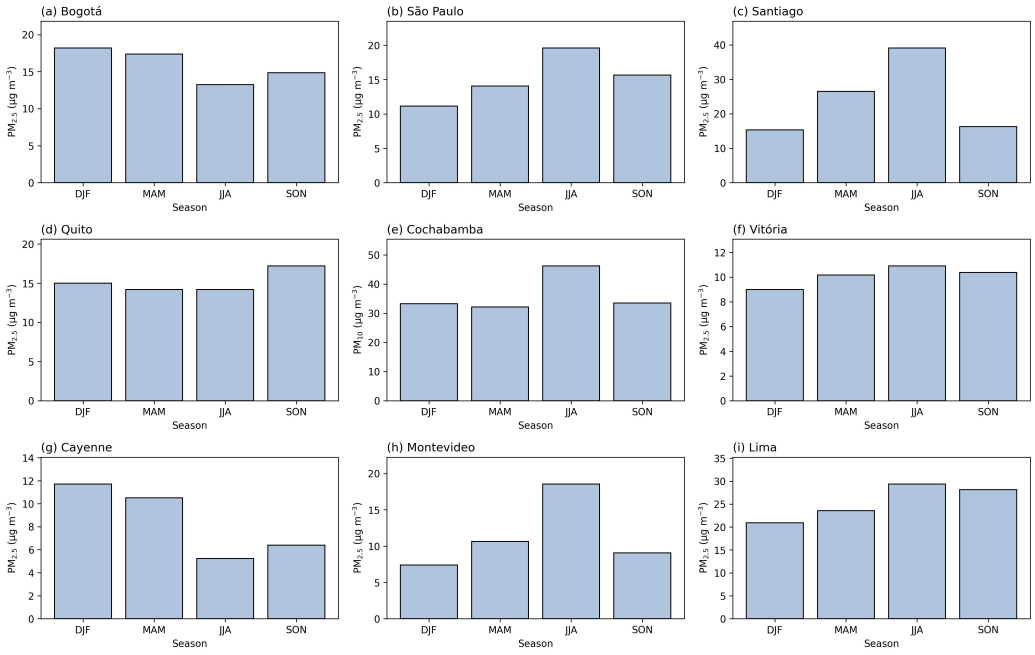



Figure S18: Multi-year seasonal mean of $PM_{2.5}$ concentrations for the nine urban locations analyzed in this study, calculated from ground stations over the period of interest (2013-2023). Each panel corresponds to one city: (a) Bogotá, (b) São Paulo, (c) Santiago, (d) Quito, (e) Cochabamba, (f) Vitória, (g) Cayenne, (h) Montevideo, and (i) Lima; bars show the mean for DJF, MAM, JJA, and SON. Values for Cochabamba correspond to $PM_{10}$.

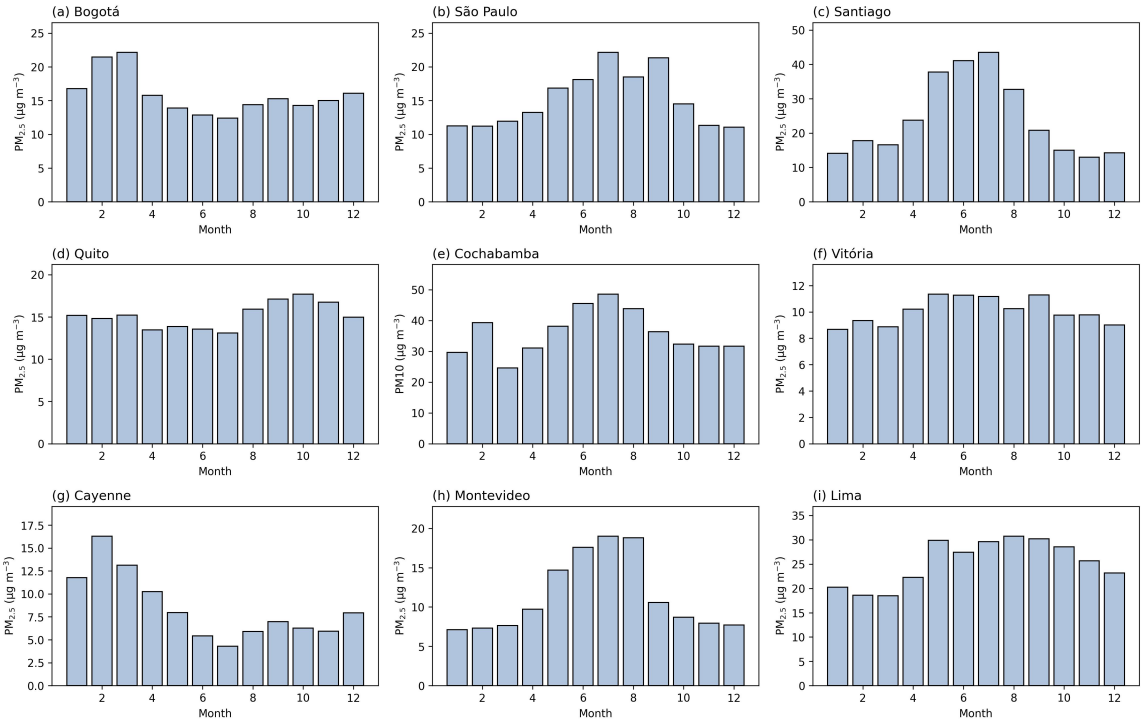



Figure S19: Multi-year monthly mean of $PM_{2.5}$ concentrations for the nine urban locations analyzed in this study, calculated from ground stations over the period of interest (2013-2023). Each panel corresponds to one city: (a) Bogotá, (b) São Paulo, (c) Santiago, (d) Quito, (e) Cochabamba, (f) Vitória, (g) Cayenne, (h) Montevideo, and (i) Lima; bars show the mean for each calendar month (1 = January, 12 = December). Values for Cochabamba correspond to $PM_{10}$.

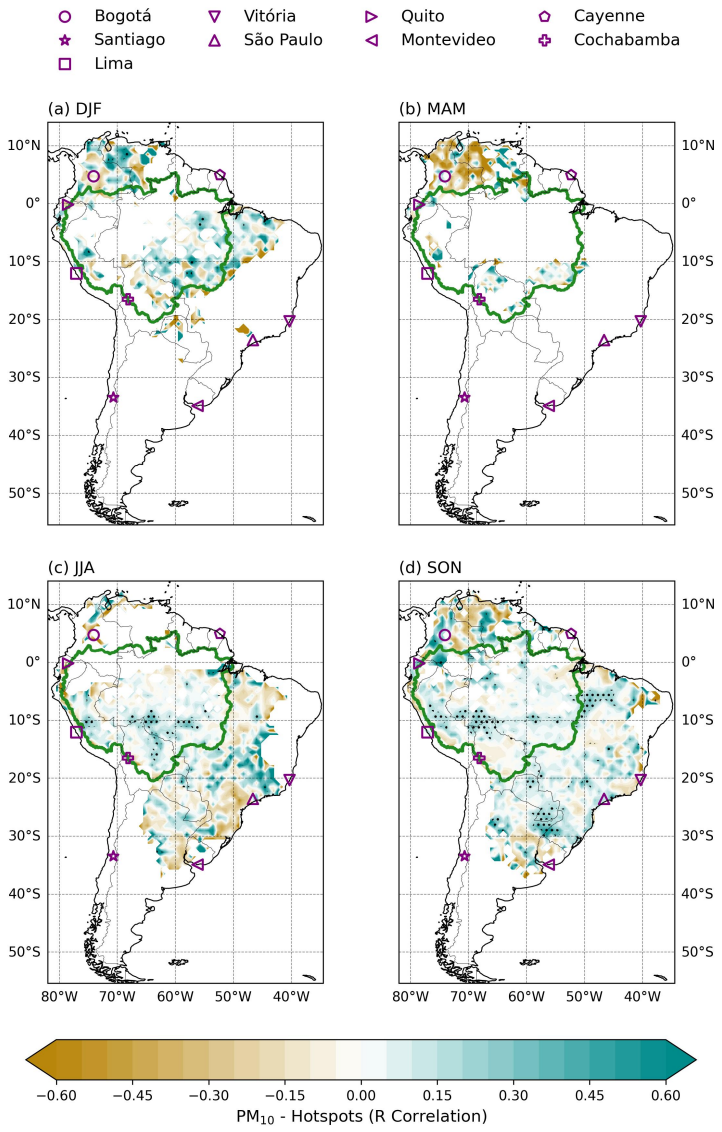



Figure S20: Seasonal Pearson correlation coefficients between $PM_{10}$ concentrations from the smoke plumes identified and fire hotspot detections across South America for (a) DJF, (b) MAM, (c) JJA, and (d) SON. Stippling denotes statistically significant correlations ($p < 0.05$). The green contour outlines the biogeographic Amazon Basin, and symbols indicate the urban locations analyzed in this study.

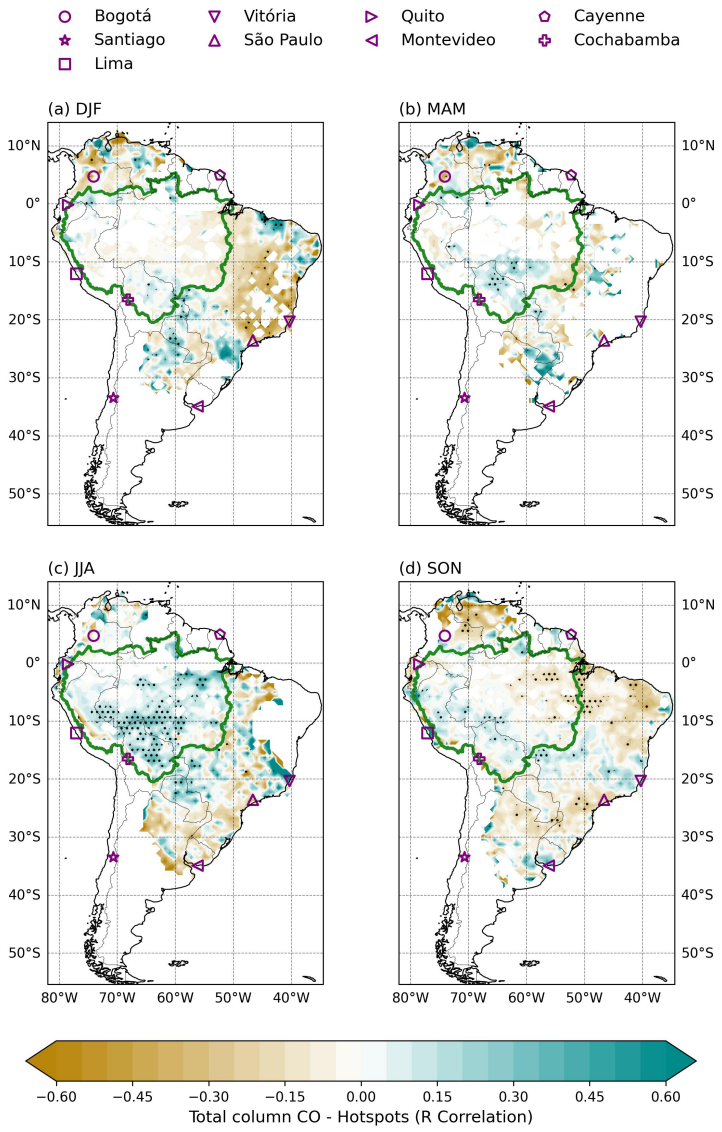



Figure S21: Seasonal Pearson correlation coefficients between TCCO concentrations from the smoke plumes identified and fire hotspot detections across South America for (a) DJF, (b) MAM, (c) JJA, and (d) SON. Stippling denotes statistically significant correlations ($p < 0.05$). The green contour outlines the biogeographic Amazon Basin, and symbols indicate the urban locations analyzed in this study.

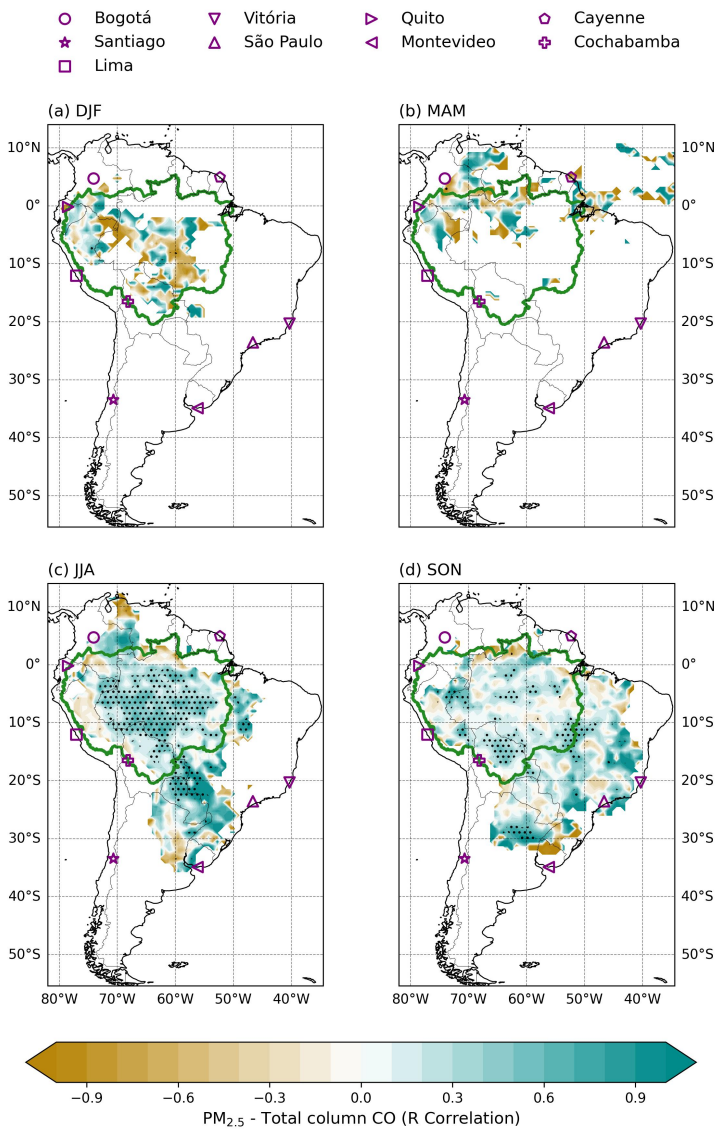



Figure S22: Seasonal Pearson correlation coefficients between TCCO and $PM_{2.5}$ concentrations from the smoke plumes identified across South America for (a) DJF, (b) MAM, (c) JJA, and (d) SON. Stippling denotes statistically significant correlations ($p < 0.05$). The green contour outlines the biogeographic Amazon Basin, and symbols indicate the urban locations analyzed in this study.

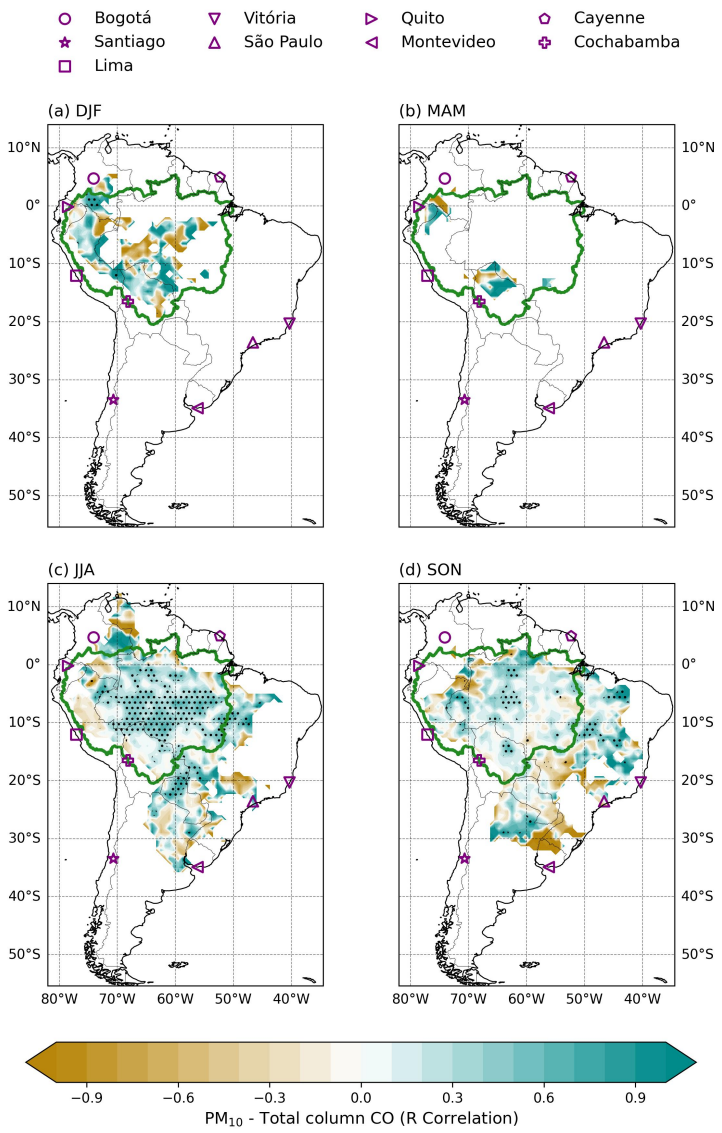



Figure S23: Seasonal Pearson correlation coefficients between TCCO and $PM_{10}$ concentrations from the smoke plumes identified across South America for (a) DJF, (b) MAM, (c) JJA, and (d) SON. Stippling denotes statistically significant correlations ($p < 0.05$). The green contour outlines the biogeographic Amazon Basin, and symbols indicate the urban locations analyzed in this study.

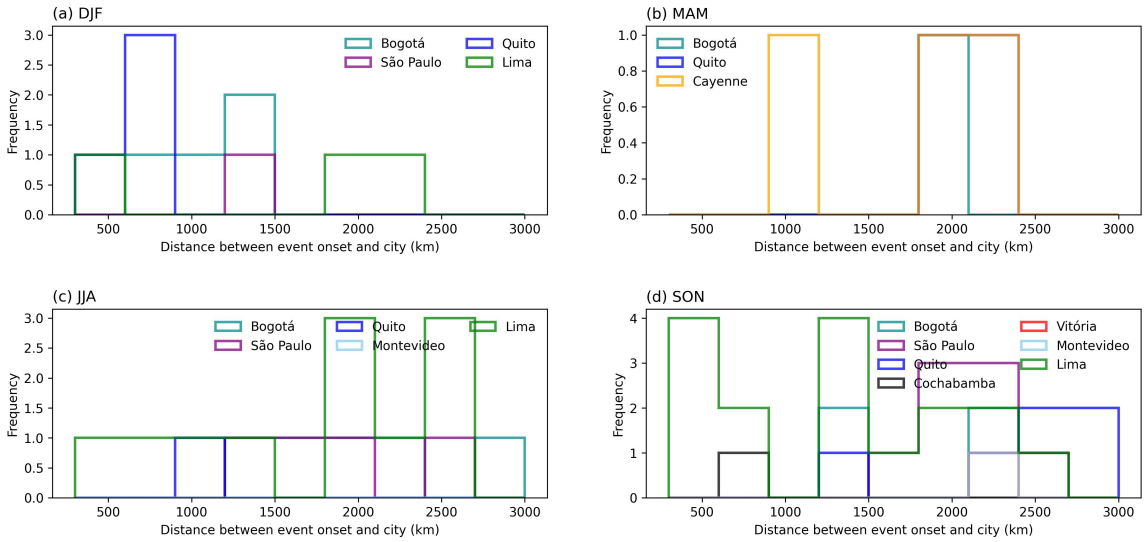



Figure S24: Seasonal distributions of transport distances between plume origin and receptor cities for Amazonian smoke events identified by the Lagrangian plume-tracking framework. Histograms show the frequency of plume events as a function of the distance between plume onset and the affected urban location for (a) DJF, (b) MAM, (c) JJA, and (d) SON. Results highlight seasonal differences in the transport pathways and spatial reach of Amazonian smoke affecting major South American cities.

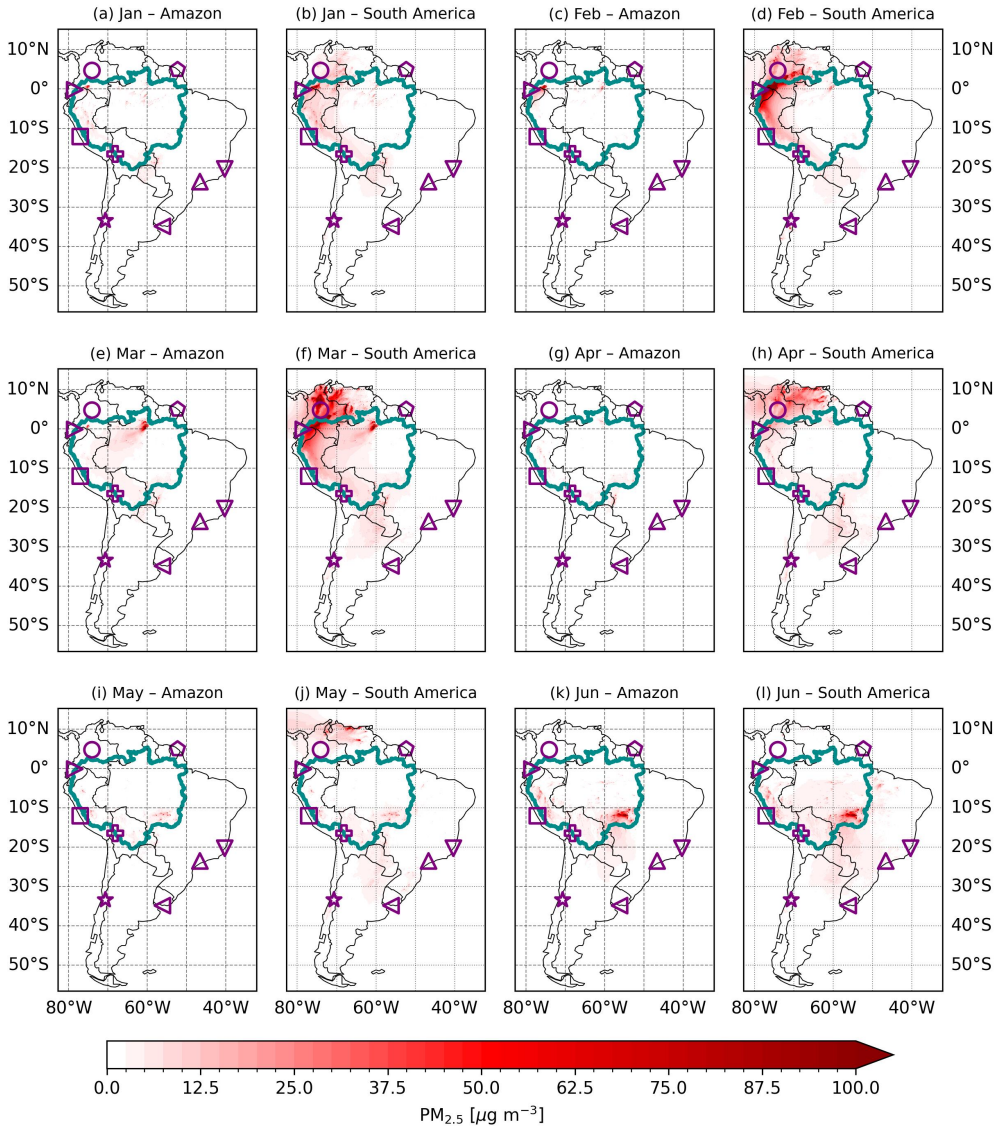



Figure S25: Monthly mean $PM_{2.5}$ concentrations attributable to Amazonian fires (Amazon) and all South American fires (South America) during January-June. Panels compare the contribution of emissions originating exclusively within the Amazon Basin with the contribution from all biomass-burning sources across South America. Panels are arranged in three rows of four; for each month, the left panel shows the Amazon contribution and the right panel the all-South-America contribution (panels a–d: January and February; e–h: March and April; i–l: May and June). The Amazon Basin is outlined in green, and symbols indicate the urban locations included in the transport, air-quality, and health-impact analyses.

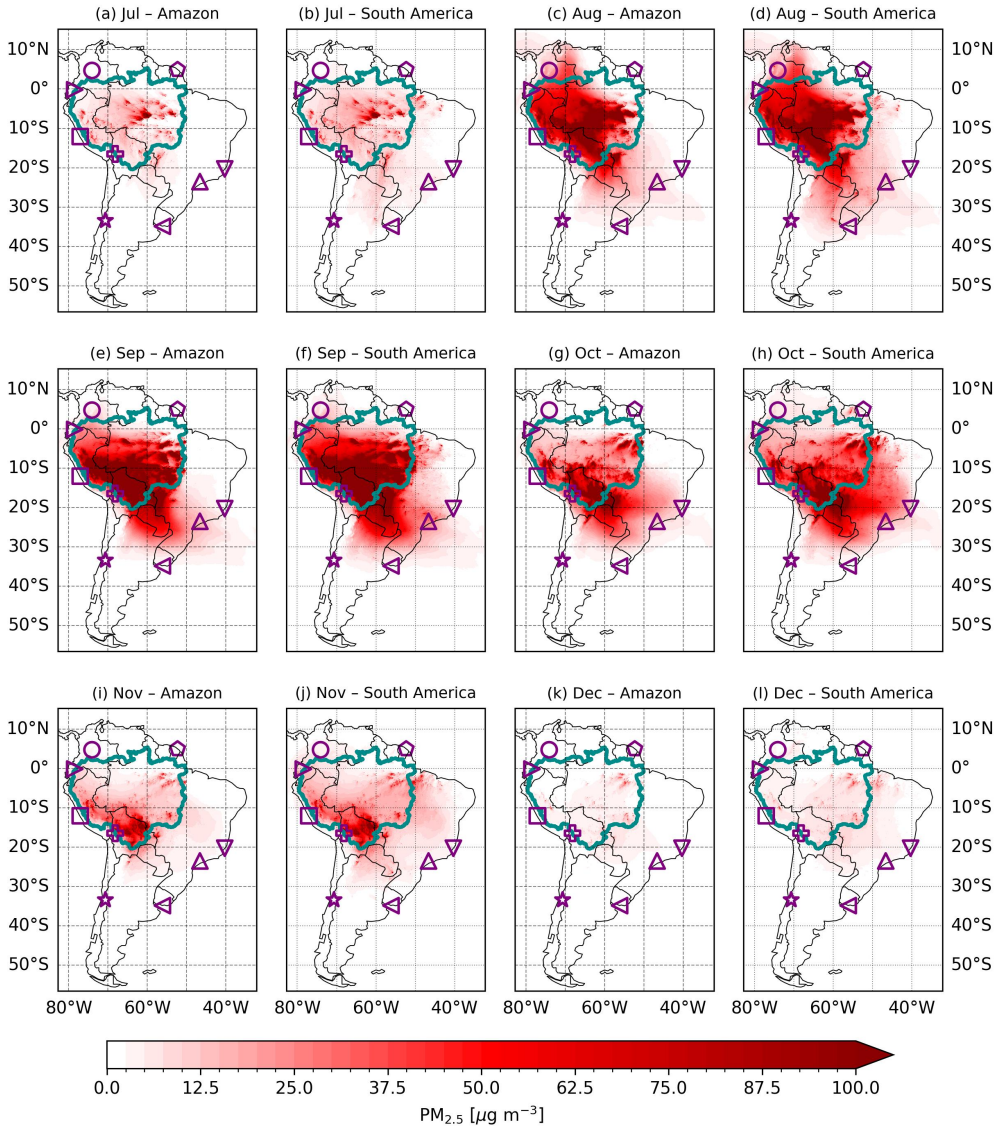



Figure S26: Monthly mean $PM_{2.5}$ concentrations attributable to Amazonian fires (Amazon) and all South American fires (South America) during July-December. Panels compare the contribution of emissions originating exclusively within the Amazon Basin with the contribution from all biomass-burning sources across South America. Panels are arranged in three rows of four; for each month, the left panel shows the Amazon contribution and the right panel the all-South-America contribution (panels a–d: July and August; e–h: September and October; i–l: November and December). The Amazon Basin is outlined in green, and symbols indicate the urban locations included in the transport, air-quality, and health-impact analyses.

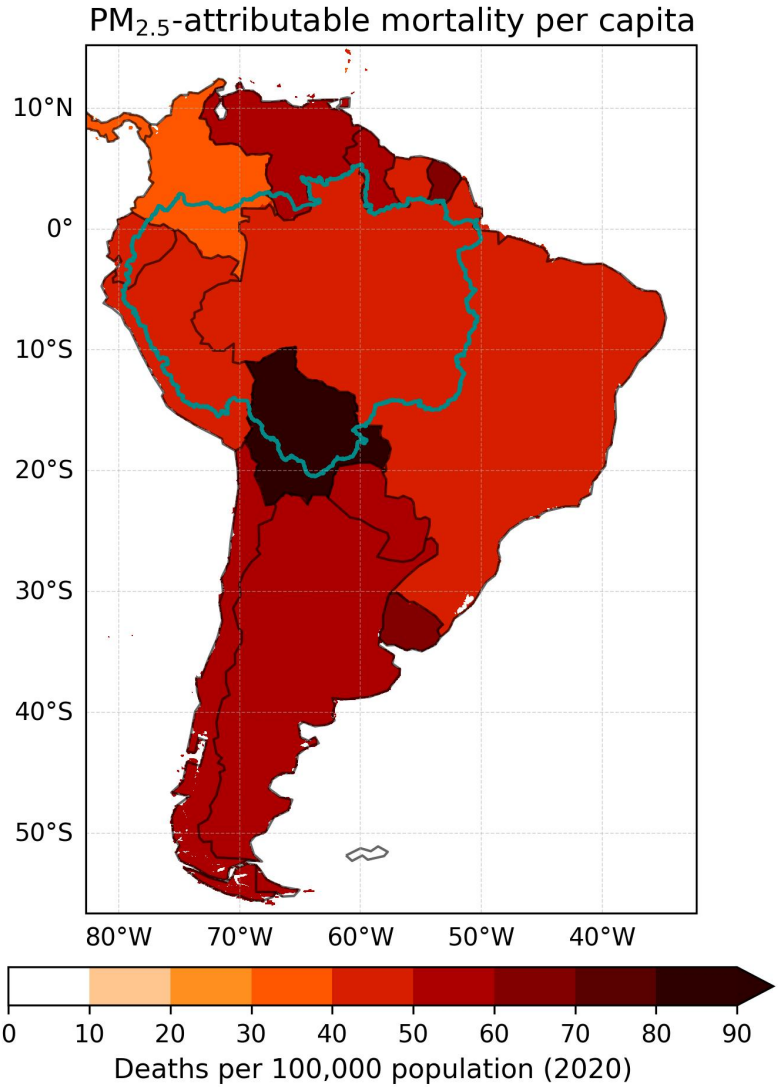



Figure S27: $PM_{2.5}$-attributable mortality per capita (deaths per 100,000 population) for the baseline reference scenario in 2020, computed as country-total attributable deaths divided by country-total population. Normalizing by population highlights countries with disproportionately large health burdens relative to their population size.

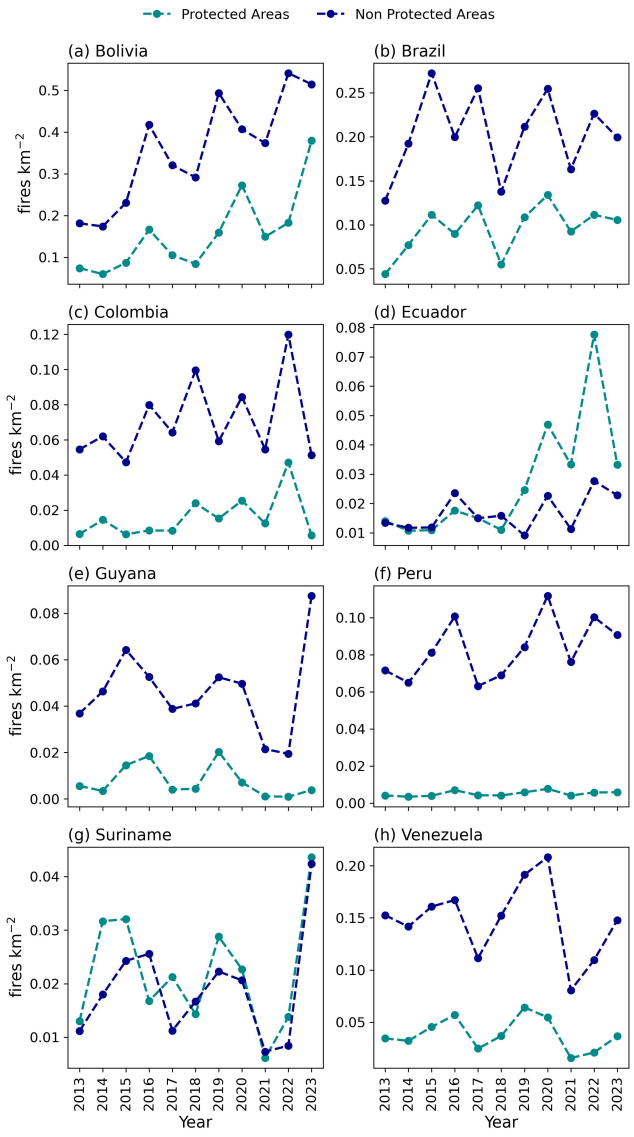



Figure S28: Yearly temporal evolution of hotspot density (active fire detections km$^{-2}$) inside protected areas (PA, green) and non-protected areas (NPA, blue) across Amazonian regions of (a) Bolivia, (b) Brazil, (c) Colombia, (d) Ecuador, (e) Guyana, (f) Peru, (g) Suriname, and (h) Venezuela during 2013–2023.